

# Study of Coating Growth Behavior During the Plasma Electrolytic Oxidation of Magnesium Alloy ZK60

Zhaozhong Qiu, Rui Wang, Yushen Zhang, Yunfei Qu, and Xiaohong Wu

(Submitted June 23, 2014; in revised form January 29, 2015; published online February 20, 2015)

Plasma electrolytic oxidation technique was used to coat ZK60 magnesium alloy in a silicate-based electrolyte. Effects of oxidation time on the morphology, phase structure, and corrosion resistance of the resulting coatings were systematically investigated by scanning electron microscopy, energy-dispersive spectrometry, x-ray diffraction, x-ray photoelectron spectroscopy, and potentiodynamic polarization. The main components of the inner and the outer coating layers were MgO and Mg<sub>2</sub>SiO<sub>4</sub>, respectively. It was also found that the oxidation time has a significant impact on the corrosion resistance properties of the coatings. The coating obtained within the oxidation time of 360 s exhibited a corrosion current of  $7.6 \times 10^{-8}$  A/cm<sup>2</sup> in 3.5 wt.% NaCl solution, which decreased significantly when comparing with the pristine magnesium alloy.

**Keywords** ceramic coatings, corrosion resistance, magnesium alloy ZK60, plasma electrolytic oxidation

## 1. Introduction

ZK60 alloy is a typical high-strength wrought magnesium alloy with good stress corrosion resistance and heat treatability (Ref 1). Furthermore, the ZK60 Mg alloy has naturally degradable property and the highest strength-to-weight ratio among all metals, and thus is considered as promising artificial bones material (Ref 2, 3). However, magnesium alloys exhibit poor corrosion resistance due to their high reactivity of the magnesium matrix (Ref 4-6), which is one of the principal obstacles in practical applications. A large number of surface modification treatments are available to address the intractable problems, such as chemical conversion coatings (Ref 7-10), vapor-phase deposition processes (Ref 11), laser surface alloying (Ref 12), organic coating (Ref 13-15), and plasma electrolytic oxidation (PEO) (Ref 16, 17). Among these techniques, PEO is a method of great significance for enhancing corrosion resistance, which can remarkably enhance the corrosion resistance by producing a moderate thick and dense solid oxide coating on the magnesium alloys (Ref 18).

Recently, particular attention has been paid to PEO treatments for the magnesium alloys. Many researchers have investigated the influences of electrolytes (Ref 19-21) and pH values during the PEO process on the corrosion of magnesium alloys (Ref 22-24). The effects of oxidation time on the corrosion resistance of PEO coatings on the magnesium alloys in NaCl solution have also been studied (Ref 25-28). According

to the literature, it can be inferred that the main components of the inner and the outer layers should also depend greatly on the oxidation time. However, studies on this point have not been carried out yet.

In this work, PEO coatings on ZK60 magnesium alloy with superior corrosion resistance properties have been prepared by a facile anodizing process. The main components of the inner and the outer layers were studied systematically. The growth characteristics and the corrosion resistance of PEO coatings obtained in Na<sub>2</sub>SiO<sub>3</sub> + KOH + NaF-based electrolyte have been discussed in detail. The relationship between the oxidation time and corrosion resistance of the coatings has also been investigated.

## 2. Experimental

### 2.1 Preparation of PEO Coatings

Rectangular coupons (25 mm × 20 mm × 5 mm) of ZK60 magnesium alloy (mass fraction: Zn 5 wt.%, Zr 0.3 wt.%, Mn 0.1 wt.% and balance Mg) were used as substrate material in this study. They were abraded with 180, 600, 1000, and 2000 grit emery sheets, respectively, and then cleaned with acetone before PEO treatment. Homemade pulsed bipolar electrical source with power of 5 kW was used for PEO in a water-cooled electro bath made of stainless steel, which also served as the counter electrode. The reaction temperature of the electrolytes during the processing was kept at  $20 \pm 5$  °C by adjusting the cooling water flow. PEO process equipment was similar to the one presented by Matthews' group (Ref 29). An aqueous electrolyte was prepared from a solution of sodium silicate (Na<sub>2</sub>SiO<sub>3</sub>·9H<sub>2</sub>O, 20 g/L), potassium hydroxide (KOH, 7 g/L), and sodium fluoride (NaF, 1 g/L). The electronic power frequency was fixed at 1000 Hz. The duty ratios of pulses were equivalent to 10%. The applied current density was 0.6 A/dm<sup>2</sup>. After PEO treatment, the samples were rinsed with deionized water and dried in the air. All experiments were carried out at room temperature and standard atmospheric pressure.

Zhaozhong Qiu, Rui Wang, Yushen Zhang, Yunfei Qu, and Xiaohong Wu, Department of Chemistry, Harbin Institute of Technology, No. 92 West Dazhi Street, Harbin 150001 Heilongjiang, P. R. China. Contact e-mail: wangrui001@hit.edu.cn.

## 2.2 Analysis of the Composition and Structure of PEO Coatings

The phase composition of the coating was investigated by x-ray diffraction (XRD) with Cu K $\alpha$  radiation (D/max-rB,  $\lambda = 1.54$ ). The surface morphology of the prepared coating was observed using scanning electron microscopy (SEM; Hitachi, SU8010) equipped with an energy-dispersive spectrum (EDS). XPS analyses were performed using a Perkin-Elmer PHI-5700 ESCA system with Al(K $\alpha$ ) x-rays (energy = 1486.6 eV). Potentiodynamic polarization experiments were performed through Princeton-4000 electrochemical analyzer. Potentiodynamic polarization curves were used to analyze the corrosive nature of the coatings prepared under different oxidation times during immersion in 3.5 wt.% NaCl solution. Each sample was mounted by paraffin with 1 cm<sup>2</sup> surface exposed. The corrosion potential and the corrosion current density were obtained through the linear analysis of Tafel approximation. All electrochemical measurements were performed with a conventional three-electrode system of coated samples as working electrode, a platinum plate as auxiliary electrode, and Ag/AgCl(sat KCl) as reference electrode.

## 3. Results and Discussion

### 3.1 Voltage-Time Response

The galvanostatic dependence of positive voltage upon the oxidation time during PEO process is shown in Fig. 1. During the PEO process, current density keeps constantly at 0.6 A/cm<sup>2</sup>, and the instantaneous variation of the voltage is recorded every 10 s. During this period, four stages could be identified (Ref 30).

As the reaction progresses, the positive voltage increases rapidly within the first 200 s. During the first 30 s, namely stage I, the voltage rises evidently following a straight line with a slope of  $\sim 10$  V/s, where no spark, but only tiny oxygen bubbles on the surface of the sample, can be observed. These phenomena indicate that the magnesium alloy matrix begins to dissolve and a thin passive film is formed on the surface of the alloy.

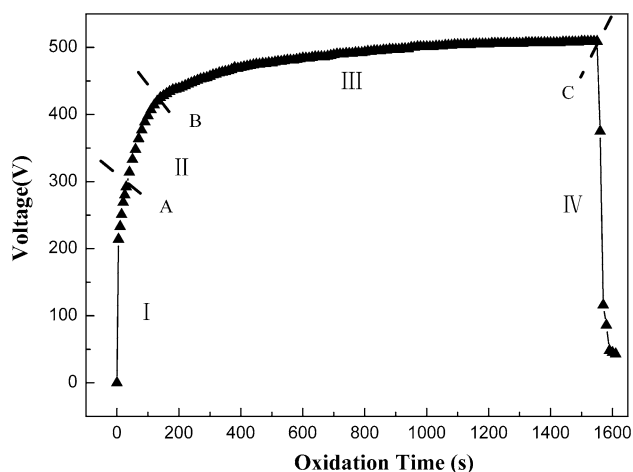


Fig. 1 Voltage-time curve of the sample during PEO process

Once the voltage exceeds a breakdown voltage (point A in Fig. 1), stage II starts, in which oxygen evolution becomes vigorous and many tiny micro-sparks occur which move on the surface of the magnesium alloy. During stage II, the cell voltage increases continually. About 130 s later (point B in Fig. 1), the voltage comes to 420 V and the oxygen evolution becomes more vigorous (Ref 30) as indicated by the appearance of buzzing orange micro-sparks. All these phenomena indicate that PEO process gets into stage III. The increase rate of the voltage decreases gradually until reaching a stable value. After 600 s, the voltage increases slightly. The micro-sparks become larger, and the sound changes from phonic to harsh in the later period of stage III. When the voltage is raised to 507 V (point C in Fig. 1), the process enters stage IV. The voltage abruptly falls to about 44 V accompanying with the disappearance of sparks and gas bubbles. As the process goes on, continuous sparking shows up at the edge of the sample, and thus the PEO process finished.

### 3.2 Phase Composition of the Coatings

XRD patterns of the oxide coatings formed in the same electrolyte for different oxidation times are shown in Fig. 2. Based on XRD patterns of PEO coatings, it could be deduced that main compositions of the coating are MgO and Mg<sub>2</sub>SiO<sub>4</sub>. The crystalline phases of the PEO coatings are Mg and a small amount of Mg<sub>2</sub>SiO<sub>4</sub> for the short oxidation time.

With increasing oxidation time, the diffraction intensities of Mg (002) and (004) peaks decrease, while the peak intensity of Mg<sub>2</sub>SiO<sub>4</sub> at 62.26° increases. The intensity of each peak is different, indicating that the components of the coatings are different. The amount of Mg decreases rapidly, and the crystal content of Mg<sub>2</sub>SiO<sub>4</sub> and MgO increases obviously with the increase of the reaction time. A quantitative phase analysis of PEO coating is performed by Rietveld analysis as shown in Table 1. The relative contents of MgO and Mg<sub>2</sub>SiO<sub>4</sub> increase as the reaction time increases, which could be attributed to the thickness of the coating.

Figure 3 shows the XPS spectra of PEO coating. It could be observed that the coating mainly consists of Mg, Si, C, Zn, and O elements. Mg and Zn elements come from Mg alloy substrate, while Si and O elements are from the electrolytes. C

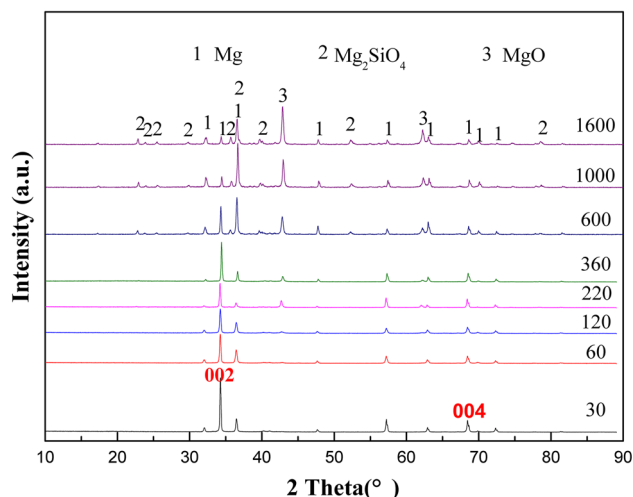


Fig.2 XRD patterns of ceramic coatings produced at different oxidation times

element is likely to be from the pollutions in the vacuum chamber during XPS test.

High-resolution spectra of Si 2p, Mg 1s, and O 1s are presented in Fig. 3(b)-(d), respectively. There are four Mg 1s component peaks in Fig. 3(c). The narrow peak (FWHM of 0.6 eV) with binding energy (BE) at 1304.67 eV is assigned to  $Mg_2SiO_4$ . The highest peak at BE 1303.80 eV is deemed to be MgO. The intermediate peak is centered at 1303 eV, indicating the co-existence of  $Mg^{2+}$ . The lowest peak at BE of 1302.20 eV is assigned to amorphous  $Mg(OH)_2$ . According to Si2p, the BE of 102.42 eV is associated with  $Mg_2SiO_4$ , indicating that the  $SiO_3^{2-}$  species in the electrolyte are incorporated into the coating during PEO process. Figure 3(d) displays O 1s XPS spectra of the coating, where oxygen peak comes from periclase (MgO) and forsterite ( $Mg_2SiO_4$ ) can be observed. The results demonstrate that the PEO coating is composed of  $Mg_2SiO_4$  and MgO, which are in accordance with the results of XRD.

Under the constant current density, an entire anodizing process can be divided into four stages based on the above findings. In the first few seconds, the anionic coacervate is formed at the magnesium/electrolyte solution boundary under the action of anodic voltage. The thickness of the coacervate rises with increasing voltage. Equation (1) takes place, and magnesium ions enters into the solution (Ref 31, 32). The interface reaction can be described as follows:



As the oxidation proceeds, the voltage attacks the homogeneous oxide coatings with the emergence of the infinitesimal arc on the sample surfaces. Sharma et al. (Ref 33) reported that

**Table 1** Quantitative analysis for the crystal phase of PEO coatings by x-ray diffraction

Oxidation time, s	Mg, wt.%	MgO, wt.%	$Mg_2SiO_4$ , wt.%
30	0.99175	0.00825	0
60	0.9578	0.0422	0
120	0.8936	0.1064	0
220	0.7232	0.2768	0
360	0.832	0.1587	0.0093
600	0.4621	0.4502	0.0877
1000	0.1942	0.6980	0.1078
1600	0.1183	0.7574	0.1243

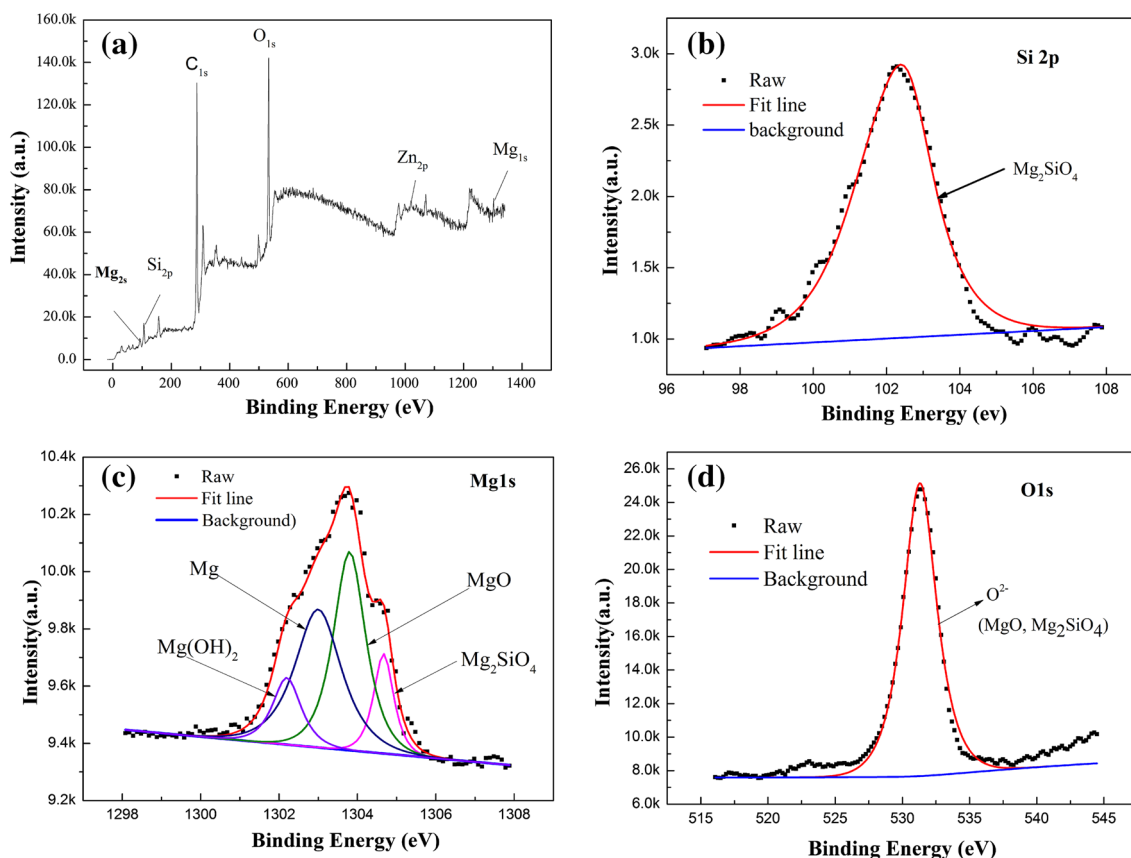


**Fig.3** XPS data of the ceramic coating on ZK60 Magnesium alloy after oxidation 1600 s, (a) whole pattern, (b) Si 2p, (c) Mg 1s, and (d) O 1s

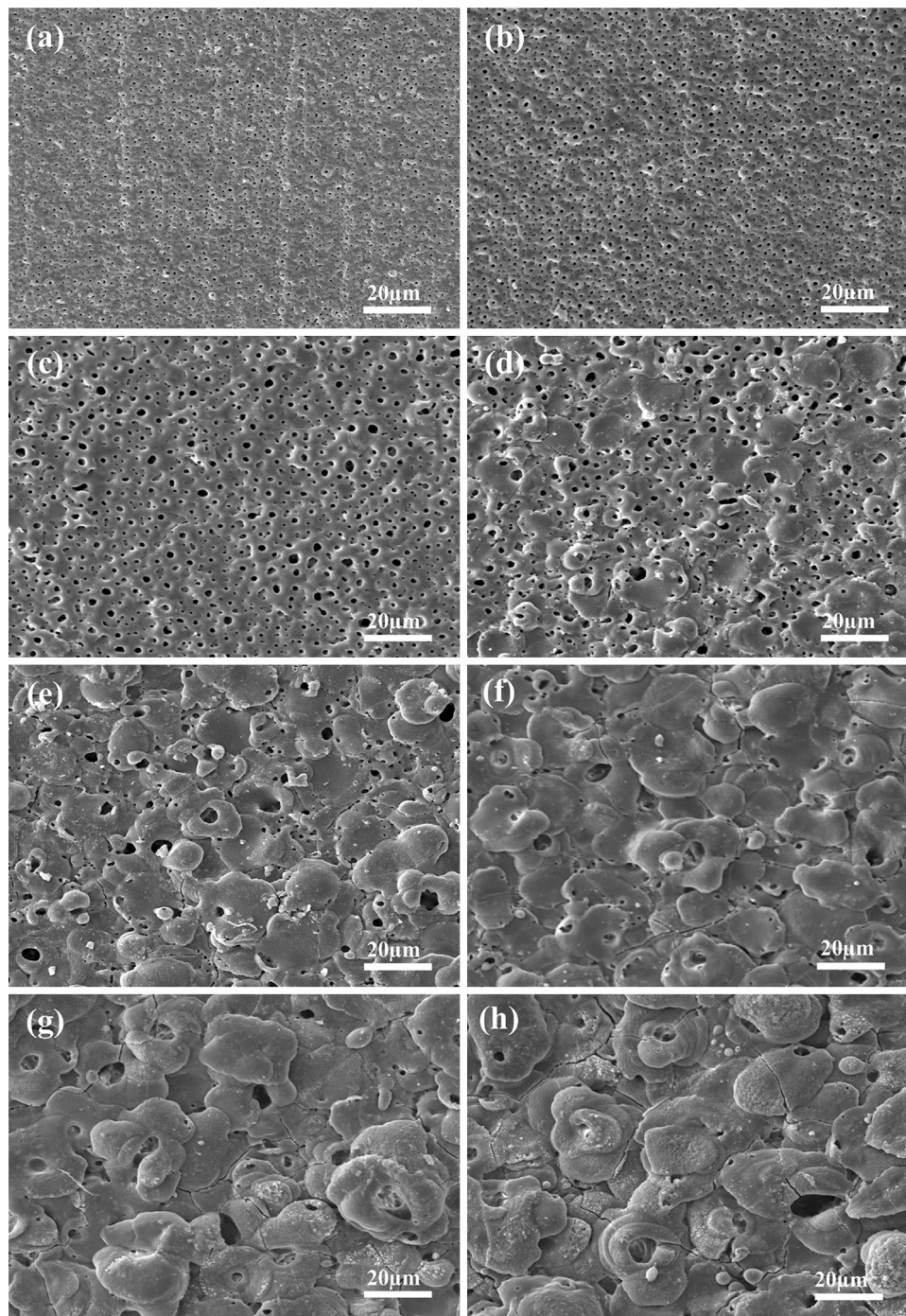
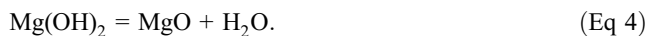


**Fig.4** Surface micrographs of the samples anodized for different times: (a) 30 s, (b) 60 s, (c) 120 s, (d) 220 s, (e) 360 s, (f) 600 s (g) 1000 s, (h) 1600 s

the dehydration reaction is thermodynamically endothermic. Because the instantaneous temperature in the micro-area is higher than 1000 °C (Ref 34),  $\text{Mg}(\text{OH})_2$  in the oxide film could be decomposed into  $\text{MgO}$  and  $\text{H}_2\text{O}$  (Ref 35):



When the voltage exceeds the breakdown value, sparks and vigorous oxygen evolution in stage II and III could be observed on the surface of the sample, indicating an increased reaction

rate of Eq (2). Oxygen could also be generated from the thermal decomposition of water (reaction 5) in the sparking areas. The increased voltage would accelerate the reaction rate. When enough magnesium ions accumulate at the magnesium/electrolyte interfaces, the magnesium ions would react with  $\text{SiO}_3^{2-}$  and  $\text{OH}^-$  in the bulk solution (reaction 6):

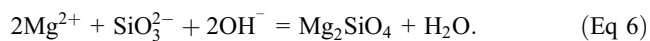


**Table 2** .The mean diameter and porosity of the samples produced at different oxidation times

Oxidation time, s	Mean diameter, $\mu\text{m}$	Porosity, $\text{N}/\text{cm}^2$
30	0.42	4032
60	0.68	2923
120	1.22	932
220	1.69	630
360	2.21	267
600	3.35	107
1000	5.62	62
1600	6.34	41

### 3.3 Changes of Coating Morphologies

According to Albella model (Ref 36), anionic species in the electrolyte such as  $\text{OH}^-$ ,  $\text{F}^-$ , and  $\text{SiO}_3^{2-}$  may enter into the oxide coating and act as impurity centers. Moreover, they can be further ionized under the high anodization field following the Poole-Frenkel mechanism, and thus release electrons into the oxide conduction band. These primary electrons are further accelerated by the applied electric field to produce electron avalanches by an impact ionization method, which subsequently leads to a critical electronic current to breakdown the coatings. Figure 4 displays the surface morphologies of PEO coatings obtained at different oxidation times. The surfaces of

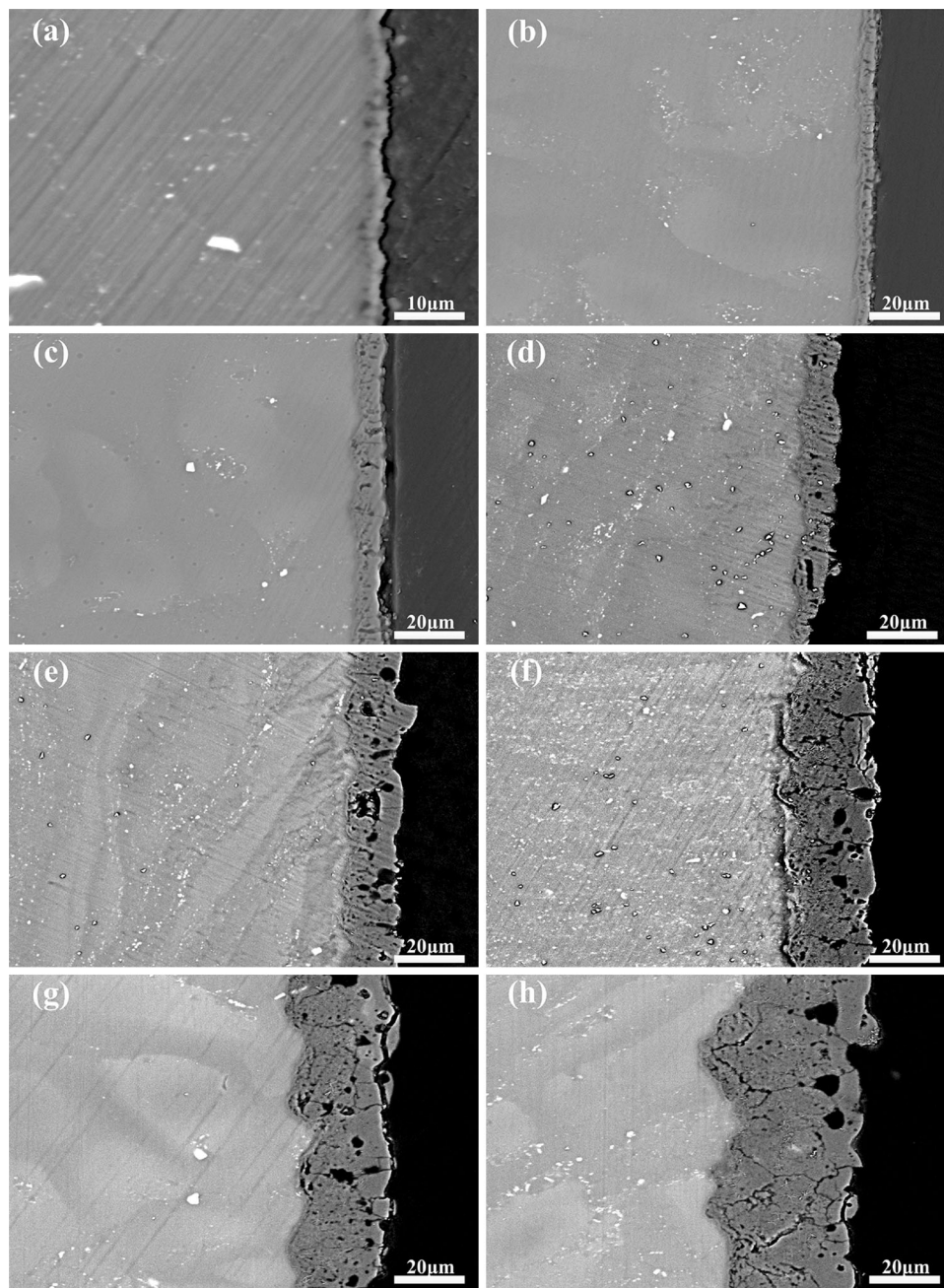


**Fig.5** Cross-section micrographs of the samples anodized for different times: (a) 30 s, (b) 60 s, (c)120 s, (d) 220 s, (e) 360 s, (f) 600 s, (g)1000 s, (h) 1600 s

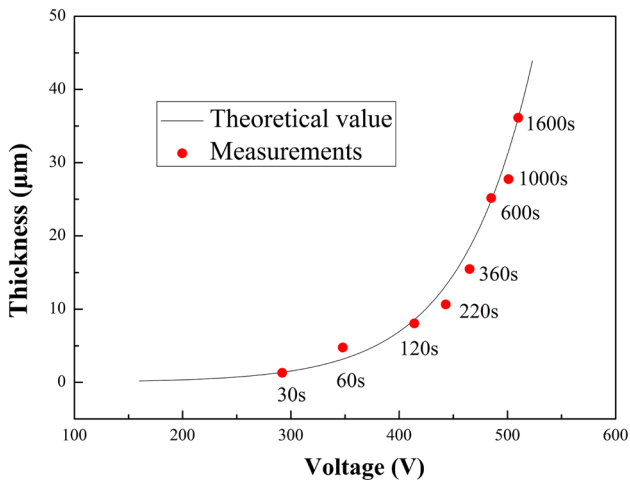


Fig.6 The thickness of ceramic coatings at different oxidation times

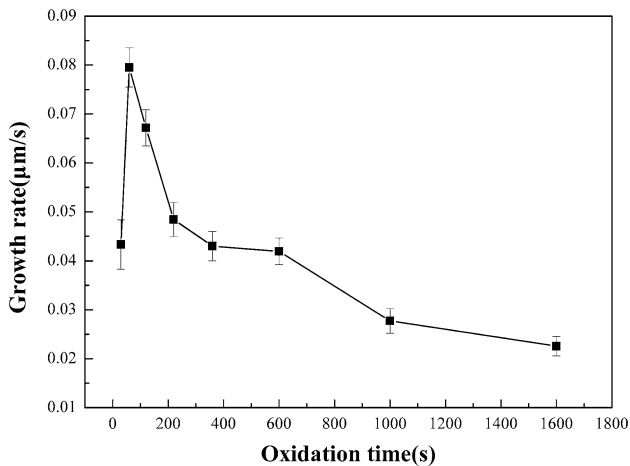


Fig.7 The growth rate of ceramic coatings at different oxidation times

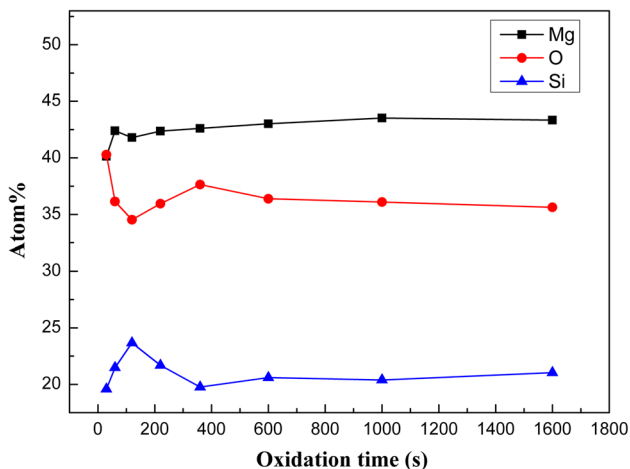


Fig.8 Variation of surface elemental concentration of the samples at different oxidation times

PEO coatings contain more or less minor level of micro-pores and some micro-cracks. As shown in Fig. 4(a) and (b), the discharge channels obtained at the oxidative time of 30 and

60 s are well distributed on the sample surfaces. The surfaces contain considerable craters (Fig. 4h), which arise from discharge energy and oxygen bubbles generated by decomposition of  $\text{OH}^-$  (Ref 37, 38) in the anodic electrode reaction (2) thrown out through the channels during PEO process.

Different shaped pores are distributed all over the surfaces. Table 2 shows the average diameters and porosity of the samples produced at different oxidation times. Obviously, the absolute number of the pores decreases, and the average diameters of the pores increase significantly increasing the oxidation time. Micro-cracks can be observed on the surfaces (Fig. 4e-h), which should be partially caused by the thermal stress formed during rapid solidification of the molten oxide when the electrolyte acts as a coolant. Moreover, the lower Pilling-Bedworth ratio (PBR) of magnesia also plays an important role in the appearance of the cracks in PEO coatings on magnesium alloys (Ref 39).

### 3.4 Cross-Section Structural Characterization

All the coatings possess a typical PEO coating characterized by the existence of the inner and outer layer. The inner layer is compact, while the outer one is relatively loose. No fracture sites can be observed in the interface between coatings and substrates, which indicates good quality adhesion between them. Thickness of the coatings is uniform, and the average thickness is about  $1 \mu\text{m}$  when the oxidation time is 30 s (Fig. 5a). It can be clearly seen that the coatings become thicker with fewer pores as the oxidation time goes on. The thickness of the coating is about  $40 \mu\text{m}$  in thickness when the oxidation time reaches to 1600 s, as shown in Fig. 5h.

The breakdown voltage has a logarithmic linear correlation with the thickness of the coatings and can be described by Eq (7), in which  $h$  is the thickness of the coating,  $h_i$  and  $k$  are constants, and  $V_B$  is the breakdown voltage (reaction 7). The growth mechanism of PEO coatings can be explained by Albella model (Ref 40). Figure 6 shows the exponential advance of thickness to the breaking voltage. The thick coating could protect the substrate from corrosion at the early stage of micro-arc oxidation. However, when the coating is thick enough, further growth of the coating becomes rather difficult, and the voltage must be increased to break the coating. The energy of single pulse can be determined by the break voltage ( $V$ ), peak currents ( $I$ ), and pulse width ( $t$ ) (Eq (8)):

$$h = h_i \times \exp[k(V - V_B)], \quad (\text{Eq } 7)$$

$$Q = \int_0^t V(t)I(t)dt. \quad (\text{Eq } 8)$$

The increasing break voltage accelerates the discharging energy, leading to the increase of product mass by a single pulse and the enlarged pore sizes after the discharged channels are cooled. The bigger pore increases the contact area between the corrosive electrolyte and the substrate, while cannot restrict the invasion of  $\text{Cl}^-$  to protect the magnesium alloy. Furthermore, the increased voltage induces the heat stress to rupture the coating consequently. In a word, the bursting of the coating loses the protective ability for the substrate markedly.

Figure 7 shows the growth rate of the coatings for different times. According to the thickness, it can be calculated that the average growth rates are  $\sim 0.80$  and  $\sim 0.023 \mu\text{m/s}$  for 60 and

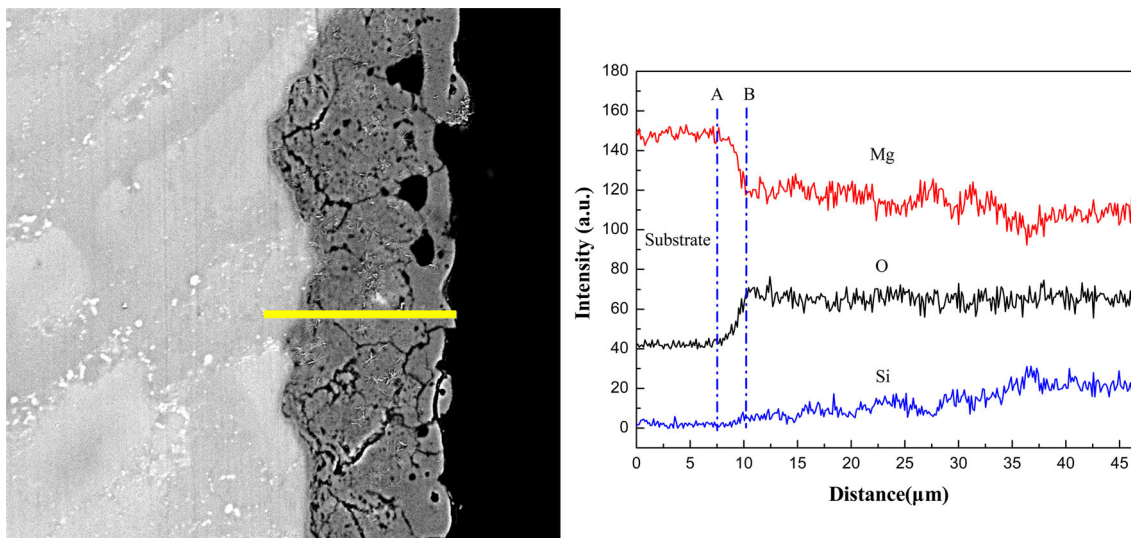


**Fig.9** Line scanning electronic microscope photograph and elements distribution of ceramic coating cross section

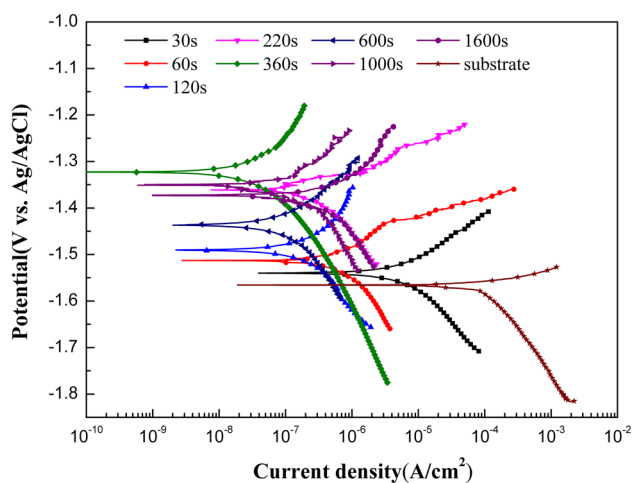


**Fig.10** Potentiodynamic polarization curves of samples with different oxidation times in the 3.5 wt.% NaCl solution

**Table 3** Corrosion current density and corrosion potential of substrate and coated samples produced at different oxidation times

Oxidation time, s	Corrosion potential, V	Corrosion current density, $\mu\text{A}/\text{cm}^2$
30	-1.54	8.264
60	-1.51	1.677
120	-1.49	0.73
220	-1.34	0.23
360	-1.32	0.076
600	-1.44	0.19
1000	-1.35	0.21
1600	-1.37	0.99
Substrate	-1.57	105

1600 s specimens, respectively. These phenomena suggest that the growth rate of the coatings is very high in the initial stages and then slows down. With increasing treatment time, the

growth of the coating increases exponentially relationship with voltage. The destructive effects (the crack) of the break voltage on the coating are primary over the protective action of the coating at the posterior part of PEO process.

### 3.5 Growth Mechanics of the Ceramic Coatings on ZK60 Magnesium Alloys

The chemical compositions of the coating surface, as determined by EDS, are shown in Fig. 8. The surface layer is primarily composed of Mg, Si, and O, associated with  $\text{Mg}_2\text{SiO}_4$  and MgO as determined by XRD. *F* is undetectable by EDS owing to its low concentration. As the oxidation time increases from 30 to 120 s, oxygen content of PEO coatings decreases and Si accumulates to be mushroom-like structure. The results indicate that a thin oxide film is formed on the surface of the magnesium alloy substrate. Compared with  $\text{Mg}_2\text{SiO}_4$ , MgO is easy to form in the surface region during the initial PEO stage. In addition, Si content is raised during the oxidation process (360 to 1600 s). The results indicate that the generation rate of  $\text{Mg}_2\text{SiO}_4$  in the ionic reaction is accelerated as the anodizing process proceeds.

Figure 9 displays line SEM photographs and elements distribution of the ceramic coating cross section. The amounts of Mg and O elements are much higher than that of Si in the inner layer. From A to B, Mg content decreases dramatically, O content increases, and Si content fluctuated and goes up gradually. Therefore, it can be deduced that MgO is preferred to be formed over  $\text{Mg}_2\text{SiO}_4$  during the initial PEO stage. With the increase of the oxidation time, the content of Si increases continuously, while Mg reduces. Ultimately, we may reach the conclusion that the composition of the outer and the inner layer is mainly  $\text{Mg}_2\text{SiO}_4$  and MgO, respectively, which is in good agreement with the results obtained from the element distribution of ceramic coating.

### 3.6 Potentiodynamic Polarizations

The potentiodynamic polarization curves of the pristine and PEO coating samples for different oxidation times in 3.5 wt.% NaCl solution are shown in Fig. 10, and relevant electro-

chemical data are listed in Table 3. These data clearly show that the corrosion resistances of these samples with and without PEO coatings are evidently different. The bare sample exhibits a corrosion current density of  $1.05 \times 10^{-4}$  A/cm<sup>2</sup> with an associated corrosion potential of  $-1.565$  versus Ag/AgCl(sat KCl). In comparison with bare sample, samples with PEO coatings exhibit more progressive corrosion potential and much lower corrosion current density, which indicates that the corrosion resistance of magnesium alloy ZK60 is improved noticeably by PEO treatment.

For the sample with PEO coatings prepared for 360 s, the corrosion potential of the coating increases, while the corrosion current density decreases to  $7.6 \times 10^{-8}$  A/cm<sup>2</sup>, which is considerably lower than that of the previous reports (Ref 41, 42). However, the corrosion current density increases with the extension of oxidation time. pH is a key factor during PEO treatment for magnesium. Using electrolyte containing a high KOH concentration provided better corrosion protection for the magnesium alloy under a corrosive environment (Ref 43). When the oxidation time increased, pH of the electrolyte comes down. Therefore, samples with PEO coatings prepared for 1600 s and the corrosion current density increases to  $9.9 \times 10^{-7}$  A/cm<sup>2</sup> revealing an accelerated corrosion rate. Hence, the optimized oxidation time of the PEO treatment is estimated to be 360 s.

## 4. Conclusion

In summary, we studied the effects of oxidation time of PEO treatment on the composition, morphology, and corrosion resistance of the coatings obtained on the surface of ZK60 magnesium alloy. The results show that MgO and Mg<sub>2</sub>SiO<sub>4</sub> are the principal ingredient of the inner and outer layers of the resulting coatings, respectively. The corrosion resistance of the coatings can be tremendously improved by optimizing the oxidation time. According to our potentiodynamic polarization curves, PEO coating obtained from the oxidation time of 360 s exhibits a corrosion current of  $7.6 \times 10^{-8}$  A/cm<sup>2</sup>, which is four orders of magnitude lower than bare ZK60 magnesium alloy.

## Acknowledgement

This work was financially supported by the National Natural Science Foundation of China (11374080).

## Reference

- Z.H. Yu, H.G. Yan, X.Y. Yin, Y. Li, and G.H. Yan, Liquefaction Cracking in Laser Beam Welded Joint of ZK60 Magnesium Alloy, *Trans. Nonferrous Met. Soc. China*, 2012, **22**, p 2891–2897
- X.H. Wu, P.B. Su, Z.H. Jiang, and S. Meng, Influences of Current Density on Tribological Characteristics of Ceramic Coatings on ZK60 Mg Alloy by Plasma Electrolytic Oxidation, *ACS Appl. Mater. Inter.*, 2010, **2**, p 808–812
- M.I. James, G. Wu, Y. Zhao, D.R. McKenzie, M.M. Bilek, and P.K. Chu, Effects of Zirconium and Oxygen Plasma Ion Implantation on the Corrosion Behavior of ZK60 Mg Alloy in Simulated Body Fluids, *Corros. Sci.*, 2014, **82**, p 7–26
- G.L. Makar and J. Kruger, Corrosion of Magnesium, *Int. Mater. Rev.*, 1993, **38**, p 138–153
- X.B. Chen, N. Birbilis, and T.B. Abbott, Effect of [Ca<sup>2+</sup>] and [PO<sub>4</sub><sup>3-</sup>] Levels on the Formation of Calcium Phosphate Conversion Coatings on Die-Cast Magnesium Alloy AZ91D, *Corros. Sci.*, 2012, **55**, p 226–232
- G. Song and A. Atrens, Recent Insights into the Mechanism of Magnesium Corrosion and Research Suggestions, *Adv. Eng. Mater.*, 2007, **9**, p 177–183
- H. Huo, Y. Li, and F. Wang, Corrosion of AZ91D Magnesium Alloy with a Chemical Conversion Coating and Electroless Nickel Layer, *Corros. Sci.*, 2004, **46**, p 1467–1477
- X.B. Chen, N. Birbilis, and T.B. Abbott, A Simple Route Towards a Hydroxyapatite-Mg(OH)<sub>2</sub> Conversion Coating for Magnesium, *Corros. Sci.*, 2011, **53**, p 2263–2268
- W. Zhou, D. Shan, E.H. Han, and W. Ke, Structure and Formation Mechanism of Phosphate Conversion Coating on Die-Cast AZ91D Magnesium Alloy, *Corros. Sci.*, 2008, **50**, p 329–337
- Y. Chen, B.L. Luan, G.L. Song, Q. Yang, D.M. Kingston, and F. Bensebaa, An Investigation of New Barium Phosphate Chemical Conversion Coating on AZ31 Magnesium Alloy, *Surf. Coat. Technol.*, 2012, **210**, p 156–165
- L. Muccioli, G. D'Avino, and C. Zannoni, Simulation of Vapor-Phase Deposition and Growth of a Pentacene Thin Film on C60 (001), *Adv. Mater.*, 2011, **23**, p 4532–4536
- X. Tong, M. Dai, and Z. Zhang, Thermal Fatigue Resistance of H13 Steel Treated by Selective Laser Surface Melting and CrNi Alloying, *Appl. Surf. Sci.*, 2013, **271**, p 373–380
- Y. Zhang, W. Cai, F. Si, J. Ge, L. Liang, C.P. Liu, and W. Xing, A Modified Nafion Membrane with Extremely Low Methanol Permeability via Surface Coating of Sulfonated Organic Silica, *Chem. Commun.*, 2012, **48**, p 2870–2872
- F. Zhang, C. Di, N. Berdunov, Y. Hu, Y.B. Hu, X.K. Gao, Q. Meng, H. Siringhaus, and D.B. Zhu, Ultrathin Film Organic Transistors: Precise Control of Semiconductor Thickness via Spin-Coating, *Adv. Mater.*, 2013, **25**, p 1401–1407
- T. Ibe, R.B. Frings, A. Lachowicz, S. Kyo, and H. Nishide, Nitroxide Polymer Networks Formed by Michael Addition: On Site-Cured Electrode-Active Organic Coating, *Chem. Commun.*, 2010, **46**, p 3475–3477
- R. Arrabal, J.M. Mota, A. Criado, A. Pardo, M. Mohedano, and E. Matykina, Assessment of Duplex Coating Combining Plasma Electrolytic Oxidation and Polymer Layer on AZ31 Magnesium Alloy, *Surf. Coat. Technol.*, 2012, **206**, p 4692–4703
- P.B. Srinivasan, C. Blawert, and W. Dietzel, Effect of Plasma Electrolytic Oxidation Coating on the Stress Corrosion Cracking Behaviour of Wrought AZ61 Magnesium Alloy, *Corros. Sci.*, 2008, **50**, p 2415–2418
- J. Liang, P.B. Srinivasan, C. Blawert, M. Stormer, and W. Dietzel, Electrochemical Corrosion Behaviour of Plasma Electrolytic Oxidation Coatings on AM50 Magnesium Alloy Formed in Silicate and Phosphate Based Electrolytes, *Electrochim. Acta.*, 2009, **54**, p 3842–3850
- Y. Wang, Z. Jiang, Z. Yao, and H. Tang, Microstructure And Corrosion Resistance Of Ceramic Coating on Carbon Steel Prepared by Plasma Electrolytic Oxidation, *Surf. Coat. Technol.*, 2010, **204**, p 1685–1688
- L. Wang, L. Chen, Z. Yan, H.L. Wang, and J.Z. Peng, Effect of Potassium Fluoride on Structure and Corrosion Resistance of Plasma Electrolytic Oxidation Films Formed on AZ31 Magnesium Alloy, *J. Alloys Compd.*, 2009, **480**, p 469–474
- H. Luo, Q. Cai, B. Wei, B. Yu, D. Li, J. He, and Z. Liu, Effect of (NaPO<sub>3</sub>)<sub>6</sub> Concentrations on Corrosion Resistance of Plasma Electrolytic Oxidation Coatings Formed on AZ91D Magnesium Alloy, *J. Alloys Compd.*, 2008, **464**, p 537–543
- M.C. Zhao, M. Liu, G.L. Song, and A. Atrens, Influence of pH and Chloride Ion Concentration on the Corrosion of Mg Alloy ZE41, *Corros. Sci.*, 2008, **50**, p 3168–3178
- J. Liang, P.B. Srinivasan, C. Blawert, and W. Dietzel, Influence of pH on the Deterioration of Plasma Electrolytic Oxidation Coated AM50 Magnesium Alloy in NaCl Solutions, *Corros. Sci.*, 2010, **52**, p 540–547
- L.O. Snizhko, A.L. Yerokhin, A. Pilkington, N.L. Gurevina, D.O. Misnyankin, A. Leyland, and A. Matthews, Anodic Processes in Plasma Electrolytic Oxidation of Aluminium in Alkaline Solutions, *Electrochim. Acta.*, 2004, **49**, p 2085–2095



25. H.M. Wang, Z.H. Chen, and L.L. Li, Corrosion Resistance and Microstructure Characteristics of Plasma Electrolytic Oxidation Coatings Formed on AZ31 Magnesium Alloy, *Surf. Eng.*, 2010, **26**, p 385–391
26. C. Blawert, V. Heitmann, W. Dietzel, H.M. Nykyforchyn, and M.D. Klapakiv, Influence of Process Parameters on the Corrosion Properties of Electrolytic Conversion Plasma Coated Magnesium Alloys, *Surf. Coat. Technol.*, 2005, **200**, p 68–72
27. Y. Gu, S. Bandopadhyay, C. Chen, Y. Guo, and C. Ning, Effect of Oxidation Time on the Corrosion Behavior of Micro-Arc Oxidation Produced AZ31 Magnesium Alloys in Simulated Body Fluid, *J. Alloys Compd.*, 2012, **543**, p 109–117
28. R.O. Hussein, D.O. Northwood, and X. Nie, The Effect of Processing Parameters and Substrate Composition on the Corrosion Resistance of Plasma Electrolytic Oxidation (PEO) Coated Magnesium Alloys, *Surf. Coat. Technol.*, 2013, **237**, p 357–368
29. A.L. Yerokhin, X. Nie, A. Leyland, A. Matthews, and S.J. Dowey, Plasma Electrolysis for Surface Engineering, *Surf. Coat. Technol.*, 1999, **122**, p 73–93
30. L. Zhao, C. Cui, Q. Wang, and S. Bu, Growth Characteristics and Corrosion Resistance of Micro-Arc Oxidation Coating on Pure Magnesium for Biomedical Applications, *Corros. Sci.*, 2010, **52**, p 2228–2234
31. H. Fukuda and Y. Matsumoto, Effects of Na<sub>2</sub>SiO<sub>3</sub> on Anodization of Mg-Al-Zn Alloy in 3M KOH Solution, *Corros. Sci.*, 2004, **46**, p 2135–2142
32. Y. Ma, X. Nie, D.O. Northwood, and H. Hu, Systematic Study of the Electrolytic Plasma Oxidation Process on a Mg Alloy for Corrosion Protection, *Thin Solid Films*, 2006, **494**, p 296–301
33. A.K. Sharma, R.U. Rani, and S.M. Mayanna, Thermal Studies on Electrodeposited Black Oxide Coating on Magnesium Alloys, *Thermochim. Acta.*, 2001, **376**, p 67–75
34. Y. Zhang, C. Yan, F. Wang, and W. Li, Electrochemical Behavior of Anodized Mg Alloy AZ91D in Chloride Containing Aqueous Solution, *Corros. Sci.*, 2005, **47**, p 2816–2831
35. R.F. Zhang and S.F. Zhang, Formation of Micro-Arc Oxidation Coatings on AZ91HP Magnesium Alloys, *Corros. Sci.*, 2009, **51**, p 2820–2825
36. J.M. Albella, I. Montero, and J.M. Martinez-Duart, A Theory of Avalanche Breakdown During Anodic Oxidation, *Electrochim. Acta.*, 1987, **32**, p 255–258
37. A.K. Vijh, Sparking Voltages and Side Reactions During Anodization of Valve Metals in Terms of Electron Tunneling, *Corros. Sci.*, 1971, **11**, p 411–417
38. A.K. Sharma, R.U. Rani, and A. Malek, Black Anodizing of a Magnesium-Lithium Alloy, *Met. Finish.*, 1996, **94**, p 16–27
39. X. Zhou, G.E. Thompson, P. Skeldon, G.C. Wood, K. Shimizu, and H. Habazaki, Film Formation and Detachment During Anodizing of Al-Mg Alloys, *Corros. Sci.*, 1999, **41**, p 1599–1613
40. K. Venkateswarlu, N. Rameshbabu, D. Sreekanth, A.C. Bose, V. Muthupandi, N.K. Babu, and S. Subramanian, Role of Electrolyte Additives on In-Vitro Electrochemical Behavior of Micro Arc Oxidized Titania Films on Cp Ti, *Appl. Surf. Sci.*, 2012, **258**, p 6853–6863
41. S. Yagi, A. Sengoku, K. Kubota, and E. Matsubara, Surface Modification of ACM522 Magnesium Alloy by Plasma Electrolytic Oxidation in Phosphate Electrolyte, *Corros. Sci.*, 2012, **57**, p 74–80
42. K.M. Lee, K.R. Shin, S. Namgung, B. Yoo, and D.H. Shin, Electrochemical Response of ZrO<sub>2</sub>-Incorporated Oxide Layer on AZ91 Mg Alloy Processed by Plasma Electrolytic Oxidation, *Surf. Coat. Technol.*, 2011, **205**, p 3779–3784
43. Y.G. Ko, S. Namgung, and D.H. Shin, Correlation Between KOH Concentration and Surface Properties of AZ91 Magnesium Alloy Coated by Plasma Electrolytic Oxidation, *Surf. Coat. Technol.*, 2010, **205**, p 2525–2531